Inorganic Chemistry

pubs.acs.org/IC Article

Structurally Precise Two-Transition-Metal Water Oxidation Catalysts: Quantifying Adjacent 3d Metals by Synchrotron X-Radiation Anomalous Dispersion Scattering

Meilin Tao,[‖] Qiushi Yin,[‖] Alexey L. Kaledin, Natalie Uhlikova, Xinlin Lu, Ting Cheng, Yu-Sheng Chen, Tianquan Lian, Yurii V. Geletii, Djamaladdin G. Musaev, John Bacsa, and Craig L. Hill*

Cite This: *Inorg. Chem.* 2022, 61, 6252−6262 Read Online

ACCESS | Metrics & More | Article Recommendations | Supporting Information

ABSTRACT: Mixed 3d metal oxides are some of the most promising water oxidation catalysts (WOCs), but it is very difficult to know the locations and percent occupancies of different 3d metals in these heterogeneous catalysts. Without such information, it is hard to quantify catalysis, stability, and other properties of the WOC as a function of the catalyst active site structure. This study combines the site selective synthesis of a homogeneous WOC with two adjacent 3d metals, $[Co_2Ni_2(PW_9O_{34})_2]^{10-}$ ($\mathbf{Co_2Ni_2P_2}$) as a tractable molecular model for CoNi oxide, with the use of multiwavelength synchrotron X-radiation anomalous dispersion scattering (synchrotron XRAS) that quantifies both the location and percent occupancy of Co (~97% outer-central-belt positions only) and Ni (~97% inner-central-belt positions only) in $\mathbf{Co_2Ni_2P_2}$. This mixed-3d-metal complex catalyzes water oxidation an order of magnitude faster than its isostructural analogue, $[Co_4(PW_9O_{34})_2]^{10-}$ ($\mathbf{Co_4P_2}$). Four independent and complementary lines of evidence confirm that $\mathbf{Co_2Ni_2P_2}$ and $\mathbf{Co_4P_2}$ are the principal WOCs and that $Co^{2+}(aq)$ is not. Density functional theory (DFT) studies revealed that $\mathbf{Co_4P_2}$ and $\mathbf{Co_2Ni_2P_2}$ have similar frontier orbitals, while stopped-flow kinetic studies and DFT calculations indicate that water oxidation by both complexes follows analogous multistep mechanisms, including likely Co−OOH formation, with the energetics of most steps being lower for $\mathbf{Co_2Ni_2P_2}$ than for $\mathbf{Co_4P_2}$. Synchrotron XRAS should be generally applicable to active-site-structure-reactivity studies of multi-metal heterogeneous and homogeneous catalysts.

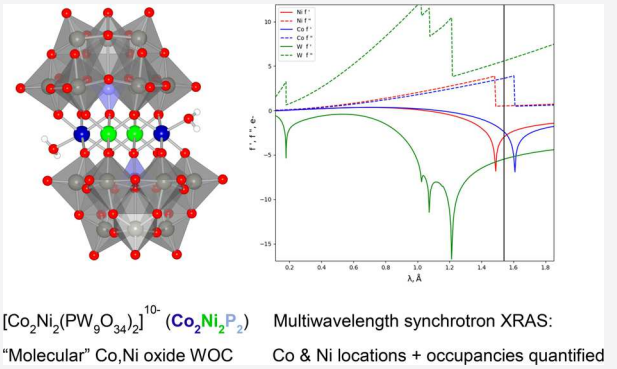

INTRODUCTION

Catalysis of water oxidation, eq 1, is central to the production of all solar fuels. Factors impacting the performance of water oxidation catalysts (WOCs) and their interfaces in electrodes and photoelectrodes remain a success-limiting factor in the low-cost production of solar fuel.[1−15]

$$2H_2O\ (\text{liquid}) \rightarrow 4e + 4H^+ + O_2\ (\text{gas}) \quad (1)$$

Some of the best WOCs are doped or mixed-metal oxides/oxyhydroxides, including cobalt-nickel mixed-metal oxyhydroxides that exhibit very high activities.[16−26] Interestingly, the cobalt and nickel centers in Co−Ni oxyhydroxides are synergistic in that these NiCoOx WOCs are more effective than cobalt oxides/oxyhydroxides or nickel oxides/oxyhydroxides alone. However, the geometric and electronic structures of these Co and Ni centers and their relationship to catalytic activity and other properties are unclear. A molecular analogue of these systems could prove to be useful in elucidating the underlying factors at play. There is a voluminous recent literature study on transition-metal-substituted polyoxometalates (POMs) used as both soluble complexes amenable to extensive molecular-level characterization and as components of anodes or photoanodes.[7,8,27−43] POM complexes are popular as WOCs because their structures and compositions can be extensively altered synthetically, yet they share the oxidative stability, low-cost, and scalability of earth-abundant-element, heterogeneous metal oxide WOCs.[44−47]

Many WOC studies probe the detailed molecular processes at or adjacent to the transition-metal active site that facilitate the four-electron, four-proton process of water oxidation (eq 1) including identification of oxidation states and potentials of the active site metals and ligand atoms likely involved in the mechanism.[4,5,13,48,49]

Received: February 9, 2022
Published: April 13, 2022

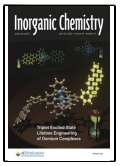

https://doi.org/10.1021/acs.inorgchem.2c00446
Inorg. Chem. 2022, 61, 6252−6262

However, there are no studies to our knowledge that assess the impact on catalytic water oxidation and WOC stability of perturbing the electronic structure of the active site by a neighboring redox-active transition metal while keeping constant the rest of the catalytic transition-metal active-site structure. This active site includes all the ligands that impact electron transfer (ET and PCET) events, counterion association, and oxygen−oxygen bond formation. The pK_a values of ligands proximal to the redox-active transition-metal active site would also ideally be kept constant. In this context, our aim was to take the much studied sandwich-type POM water oxidation catalyst, $\mathbf{Co_4P_2}$, (Figure 1, left)[7,30,31,36,37,50] and replace the two

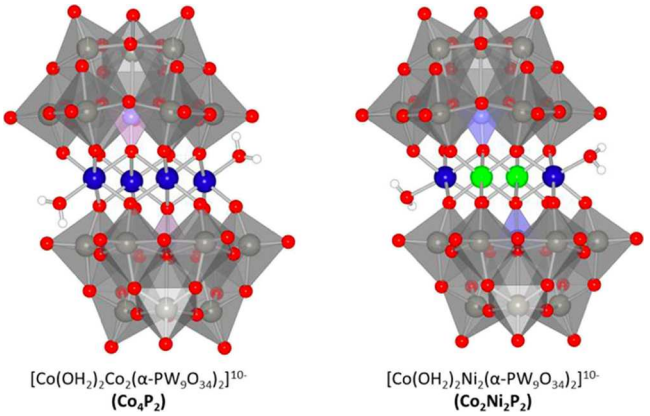

Figure 1. Structures of polyoxometalate water oxidation catalysts that have the same cobalt active site structures, overall structures, and molecular charges: $\mathbf{Co_4P_2}$ and $\mathbf{Co_2Ni_2P_2}$. Co: blue; Ni: green; WO_6: gray octahedra.

internal, solvent-inaccessible metals in the central belt (the two internal Co(II) centers in $\mathbf{Co_4P_2}$), with another redox-active transition metal, and then quantify the impact of this isomorphous, isostructural, and iso-charge replacement on the properties, including but not limited to the catalytic water oxidation turnover rate, on the exposed active-site cobalt centers. This requires a synthesis leading to these sandwich POMs with two different transition metals installed selectively at different sites. We focus on $\mathbf{Co_2Ni_2P_2}$ (Figure 1, right) that contains two nickels in place of the internal cobalts in the parent WOC, $\mathbf{Co_4P_2}$ (Figure 1, left), as this would be a molecular model of Co−Ni mixed oxide, one of the most effective heterogeneous WOCs known.[6,51,52] At the same time, the active sites in $\mathbf{Co_2Ni_2P_2}$ and those in $\mathbf{Co_4P_2}$ would have essentially congruent cobalt-active-site geometries, both having $Co(H_2O)$-(POM-oxygen)$_5$ octahedra with very similar bond distances, angles, and negative charge densities (both $\mathbf{Co_2Ni_2P_2}$ and $\mathbf{Co_4P_2}$ polyanions bear a 10− charge in their resting oxidation states). The only difference in the two WOCs is the phenomenon we are targeting—isostructural replacement of the internal transition metals in the central belt with another transition metal. Since the internal Ni(II) centers in the central belt of $\mathbf{Co_2Ni_2P_2}$ are buried, they cannot participate directly in the bond breaking and forming steps in water oxidation. These central Ni(II) centers, however, can in principle, impact catalysis and other properties, such as the nature and energies of the frontier orbitals, the hydrolytic stability, and the spectroscopy of these POM WOCs.

The focus of this study is to quantify both the position and the percent occupancies of each 3d metal in POM or in heterodinuclear di-3d-metal complexes in general. This information is needed for a quantitative comparison of the WOC and other properties of $\mathbf{Co_2Ni_2P_2}$ versus $\mathbf{Co_4P_2}$. There are organometallics,[53−55] coordination compounds,[56−60] nanomaterials,[61,62] and POMs[63−65] that contain two different metals. For some of these compounds, there is a sufficient separation distance and/or a difference in metal Z value (electron density) in which conventional fixed-wavelength X-ray crystallography can distinguish the two metals reasonably well. This is the case, for example, with the sandwich complexes, $M'_2M_2(PW_9O_{34})_2^{12-}$, where M′ = Na or Li and M = Mn^{2+}, Co^{2+}, Ni^{2+}, and Zn^{2+} because the alkali metals and the 3d transition metals have greatly different electron densities. However, this is not the case for hetero-di-3d-metal complexes.[63] Frenkel has successfully applied XANES and EXAFS to provide some structural information on two different proximal metals in nanomaterials,[62] but again, distinguishing two 3d metals that are proximal in the periodic table and proximal structurally inside the material is problematic. Mbomekallé and co-workers reported Wells−Dawson tungstoarsenates containing both Co^{II} and Fe^{III} centers[65] and thoroughly characterized them by X-ray crystallography, elemental analysis, and magnetism. However, being able to unequivocally locate and also give the percent occupancies of two adjacent 3d metals requires another technique. Thus, we report here the use of multi-

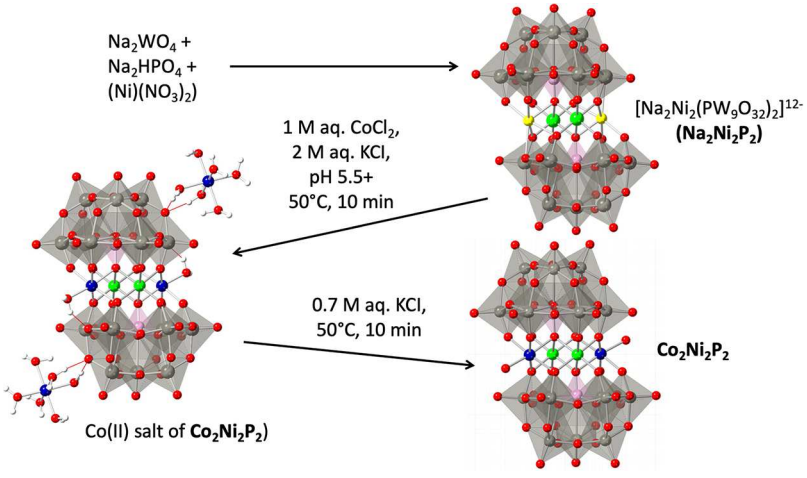

Figure 2. Synthesis of a two-transition-metal POM water oxidation catalyst.

https://doi.org/10.1021/acs.inorgchem.2c00446
Inorg. Chem. 2022, 61, 6252−6262

wavelength synchrotron X-radiation anomalous dispersion scattering (synchrotron XRAS) that does provide this information, and specifically the occupancies of both Co(II) and Ni(II) in the two crystallographically distinct sites in $\mathbf{Co_2Ni_2P_2}$. Extensive kinetics in combination with DFT calculations reveal the profound impact of the Ni-for-Co replacement on the electronic structure and WOC activity of $\mathbf{Co_2Ni_2P_2}$ versus $\mathbf{Co_4P_2}$ and other impacts of this type of selective WOC modification.

RESULTS AND DISCUSSION

Synthesis of Two-Transition-Metal Sandwich POMs. The strategy for making this two-3d-metal POM involves three steps (Figure 2). All three POM structures in Figure 2 are the X-ray structures. A reaction with the sodium salt of both tungstate and phosphate with nickel nitrate yields the structural analogue of $\mathbf{Co_4P_2}$, namely, $[Na_2(Ni)_2(PW_9O_{34})_2]^{12-}$ ($\mathbf{Na_2Ni_2P_2}$), a complex with exchangeable sodium centers on the outside of the central belt and Ni(II) centers installed in the internal, buried positions. The occupancy of the Na and Ni centers is satisfactorily confirmed by single-crystal X-ray diffraction because Na and Ni(II) have sufficiently different electron densities, a situation similar to that in the $[(NaOH_2)_2Co^{II}_2(As_2W_{15}O_{56})_2]^{18-}$ complex of Mbomekallé and co-workers.[63] In the second step, treatment of $\mathbf{Na_2Ni_2P_2}$ with Co(II) salts ($CoCl_2$ works satisfactorily) at pH 5.5 in the presence of KCl forms $\mathbf{Co_2Ni_2P_2}$ in good yield but with $[Co(H_2O)_6]^{2+}$ counterions. These counter-cations refine well crystallographically and are evident in Figure 2 (lower left structure). However, these counter-cations must be removed because hydrated divalent cobalt ions form multi-cobalt polyhydroxo complexes that are very good WOCs and would thus interfere with the comparison of the activities of $\mathbf{Co_2Ni_2P_2}$ and other WOCs. The third step involves slow re-crystallization from concentrated (0.27 M) KCl, which replaces the $[Co(H_2O)_6]^{2+}$ counterions with K^+ ones. The single-crystal X-ray diffraction (*vide infra*), elemental analysis (Table S1), and the TGA results indicate that the complete structural formula of the ion-exchanged complex (after step 3), including final crystallization, is a mixed potassium, sodium salt: $K_8Na_2Co_2Ni_2P_2W_{18}O_{68}\cdot 30H_2O$ ($KNa\mathbf{Co_2Ni_2P_2}$; see the Methods section).

Structures. The X-ray crystal structures of $\mathbf{Co_2Ni_2P_2}$ both with and without $[Co(H_2O)_6]^{2+}$ counterions (Figure 2; lower left and lower right, respectively) reveal that the $\mathbf{Co_2Ni_2P_2}$ polyanion consists of two trivacant B-α-$[PW_9O_{34}]^{9-}$ Keggin moieties with four 3d transition metals in the central belt, the classical sandwich polyanion structure first reported by Weakley et al. in 1972,[66] and appearing in scores of publications since. The refinement strongly suggests that this central belt contains two chemically equivalent Ni(II) centers in the internal positions of this C_i symmetry polyanion and two chemically equivalent Co(II) centers in the external, solvent-accessible positions defining a rhomb-like Co_2Ni_2 tetrad (Figure 1 right and Figure 2 bottom structures). Each Co^{2+} ion in $\mathbf{Co_2Ni_2P_2}$ coordinates to six oxygen atoms of the two B-α-$[PW_9O_{34}]^{9-}$ units. However, single wavelength X-ray diffraction with normal sources cannot unequivocally distinguish two 3d metals that are adjacent in the periodic table, such as Co and Ni, and proximal to one another as in mixed-3d-metal oxide WOCs or the POM analogue, $\mathbf{Co_2Ni_2P_2}$. Even less viable with conventional X-ray crystallography is the ability to quantify how much of each 3d metal is in each symmetry-distinct site, hence the main thrust of this paper.

Infrared Spectra of Conventional and Two-Metal Sandwich POMs. To assess if the FTIR spectra could distinguish these two classes of sandwich POMs, the conventional polyanion with four identical transition metals in the central belt of the complex, from the new two-transition-element sandwich POM, the FTIR spectra of $\mathbf{Co_4P_2}$ and $\mathbf{Co_2Ni_2P_2}$ in the P−O, W−O, and W−O−W stretch regions were compared (Figure 3). These regions are very similar, strongly suggesting

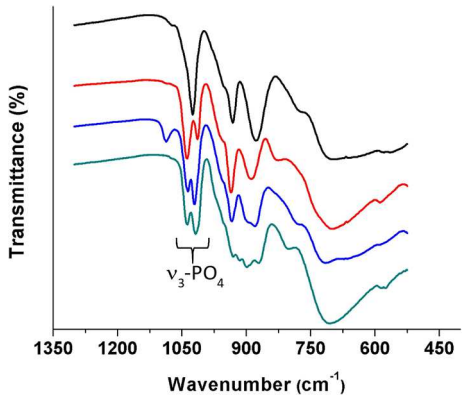

Figure 3. Comparison of the FTIR spectra. $\mathbf{Co_4P_2}$ (black), $\mathbf{Co_2Ni_2P_2}$ (red), $\mathbf{Ni_4P_2}$ (blue), and $\mathbf{Na_2Ni_2P_2}$ (green).

that the two complexes are isostructural to one another overall. However, the triply degenerate ν_3 vibrational mode of the central PO_4 unit in $\mathbf{Co_4P_2}$, labeled in Figure 3, is broadened but not split, whereas it is split in $\mathbf{Co_2Ni_2P_2}$ and in the (alkali metal)$_2$(transition metal)$_2$ precursor complex, $\mathbf{Na_2Ni_2P_2}$, indicating a greater structural distortion and a consequent lowering of the symmetry around this central heteroatom unit in the latter two polyanions. The peaks in the low energy (<1000 cm^{-1}) region are attributed to the characteristic $\nu(W{-}O_d)$, $\nu(W{-}O_b{-}W)$, and $\nu(W{-}O_c{-}W)$ absorptions, where O_b = double-bridging oxygen, O_c = central oxygen, and O_d = terminal oxygen. However, this common technique cannot tell where two different 3d metals are and certainly not to what extent.

Synchrotron XRAS to Quantify Positions and Percent Occupancies of Two 3d Metals in $\mathbf{Co_2Ni_2P_2}$. Quantitative assessment of the impact of metal(s) adjacent to the catalytic-active-site 3d metal on all the properties of this catalytic metal site requires knowledge of the positions of both the active-site metal and the adjacent 3d metal as well as their occupancies in each position. It is clear from other data in this study and conventional wisdom from many literature studies that such assignments in all oxygen−ligand environments, including mixed-metal oxide or mixed-metal POM WOCs, are very difficult with existing physical methods. In addition, $\mathbf{Co_2Ni_2P_2}$ contains 18 heavily scattering tungsten that are particularly problematic for distinguishing different adjacent 3d metals even with recent conventional X-ray diffractometers equipped with strong X-ray sources and improved detectors. As a consequence, we turned to the use of synchrotron XRAS with data collected at the Advanced Photon Source (APS) at Argonne National Laboratory to address this conundrum that is ideally suited to quantify both the location and the abundance of the two belt-transition-metals, Co and Ni, in $\mathbf{Co_2Ni_2P_2}$. The synchrotron source was necessary for purposes of both incident-wavelength tunability and intensity.

https://doi.org/10.1021/acs.inorgchem.2c00446
Inorg. Chem. 2022, 61, 6252−6262

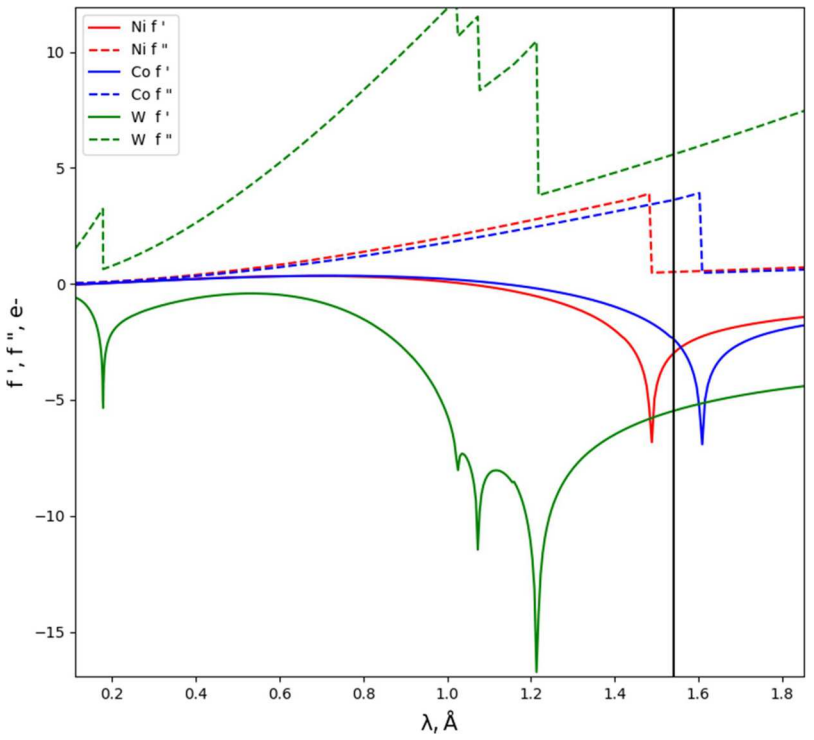

Figure 4. Resonant scattering signals for W, Ni, and Co in $Co_2Ni_2P_2$ used by GSAS-II[67] for multi-wavelength refinements of the XRAS data. The M^{II} = Co, Ni atom site fractions were refined with the resonant data. The 30 keV data was used to provide the best atomic and thermal motion model. Subsequently, the entire structure along with the optimized site fractions was refined on all the data to provide the best overall results.

In conventional X-ray diffraction, the intensities are proportional to the structure factors, |F(hkl).[2]. If the nature of the scattering, including any phase changes, is identical for all atoms, then |F(hkl)| = F(-h-k-l) (Friedel's law) holds. The imaginary component of the atomic scattering factor (third term in eq 2) has a phase that lags $\pi/2$ behind that of the primary wave. Introduction of the real and imaginary components causes Friedel's law to break down and gives rise to intensity differences or signals that can be used to locate the anomalous scatterers. By varying the wavelength, the differences can be used to identify different elements in the molecule because every element in a crystal has its own, unique absorption K edge (illustrated in Figure 4). We collected XRAS data at the APS over a wide range of incident energies that included the two K-edges of cobalt and nickel and data to either side of the two K-edges (Figure 4).

$$f = \mathrm{fo} + \Delta f' + i\cdot\Delta f'' \quad (2)$$

The program GSAS-II[67] facilitated the use of all the multiple wavelength data to refine the populations of cobalt and nickel atoms at these specific metal sites. High-resolution data (30 keV) gave us an optimal structural model for the refinement of the fractions of both metals. The results are presented in Table 1. In short, the Co(II) and Ni(II) centers are confirmed to be located in 97 and 96% in the outer solvent-accessible and inner solvent-inaccessible positions of the central belt of $Co_2Ni_2P_2$, respectively (Figure 1, right). More details on the XRAS technique applied to this problem and all the multiwavelength data and refinements are available in the Supporting Information.

Table 1. GSAS-II Refinement Results of $Na_2K_8Co_2Ni_2P_2W_{18}O_{68}\cdot 30H_2O$

outer M atoms	inner M atoms
Co 0.97(1)	Ni 0.96(1)
Ni 0.03(1)	Co 0.04(1)

Catalyzed Water Oxidations by a Sacrificial Electron Acceptor. The catalytic efficiencies of Co_4P_2, Ni_4P_2, $Na_2Ni_2P_2$, and $Co_2Ni_2P_2$ for water oxidation were evaluated under dark homogeneous, photo-driven homogeneous and electrocatalytic conditions. The dark reactions used $[Ru(bpy)_3](ClO_4)_3$ as a stoichiometric oxidant, eq 3, and were monitored by the UV−vis spectroscopic kinetics of $[Ru(bpy)_3]^{3+}$ (ε_{670} = 420 M^{-1} cm^{-1})[68] consumption in 80 mM borate buffer at pH 8.0 using the stopped-flow technique.

$$4[Ru(bpy)_3]^{3+} + 2H_2O \rightarrow 4[Ru(bpy)_3]^{2+} + O_2 + 4H^+ \quad (3)$$

Typical kinetic curves, shown in Figure 5, are not exponential. The addition of 1.0 μM $Co_2Ni_2P_2$ results in almost complete $[Ru(bpy)_3]^{3+}$ consumption in less than 0.5 s, which is an order of magnitude faster than with 1.0 μM Co_4P_2 and more than 60 times faster than the self-decomposition rate of $[Ru(bpy)_3]^{3+}$, also shown in Figure 5. For comparison, we also recorded the kinetics of $[Ru(bpy)_3]^{3+}$ reduction catalyzed by 5 μM $Co(NO_3)_2$ (brown) and by 5 μM $Na_2Ni_2P_2$ (green). The oxygen yields, based on the initial concentration of the oxidant, $[Ru(bpy)_3^{3+}]$, increase with catalyst concentrations and reach a plateau of about 70−80% at 5.0 μM catalyst ($Co_2Ni_2P_2$ or Co_4P_2). In the presence of Ni_4P_2 or Na_2Ni_2P, the rate of $[Ru(bpy)_3]^{3+}$ consumption is the same as in the absence of a catalyst.

Light-Driven Catalytic Water Oxidation. The activity of $Co_2Ni_2P_2$ in visible-light-driven catalytic water oxidation was assessed using a standard approach with $[Ru(bpy)_3]Cl_2$ as the photosensitizer and persulfate, $Na_2S_2O_8$, as a sacrificial electron

https://doi.org/10.1021/acs.inorgchem.2c00446
Inorg. Chem. 2022, 61, 6252−6262

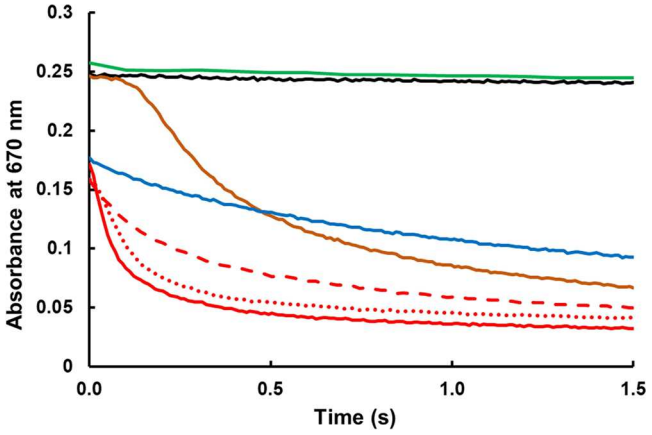

Figure 5. Kinetics of $[Ru(bpy)_3]^{3+}$ reduction measured as the decrease in absorbance at 670 nm. Black, no catalyst; green, 5 μM $\mathbf{Na_2Ni_2}$; brown, 5 μM $Co(NO_3)_2$; blue, 1 μM $\mathbf{Co_4P_2}$; and red, 1 μM $\mathbf{Co_2Ni_2P_2}$, with 0 (solid), 9 μM bpy (dotted), and 40 μM bpy (dashed); conditions: 0.43 mM (red and blue) or 0.6 mM $[Ru(bpy)_3]^{3+}$ (brown, black, and green), 80 mM sodium borate buffer at pH 8.0, 298 K.

acceptor (Figure 6).[69,70] The initial rate of O_2 formation is commonly, but incorrectly, considered as a direct measure of the

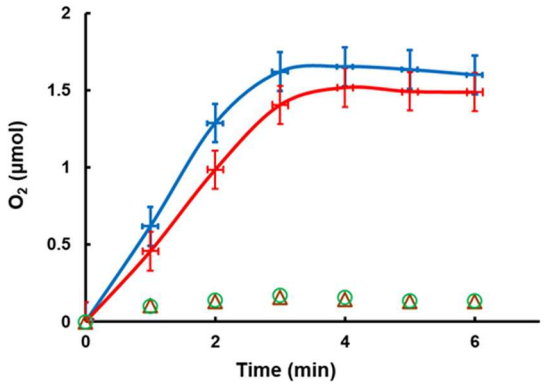

Figure 6. Kinetics of O_2 evolution in the light-driven reactions. Conditions: 1.0 mM $[Ru(bpy)_3]Cl_2$ and 5.0 mM $Na_2S_2O_8$ catalyzed by 10 μM of $\mathbf{Co_2Ni_2P_2}$ (blue), $\mathbf{Co_4P_2}$ (red), $\mathbf{Ni_4P_2}$ (green), and $\mathbf{Na_2Ni_2P_2}$ (brown). Conditions: 455 nm LED light (17 mW, beam diameter *ca.* 0.4 cm), 80 mM sodium borate buffer, initial pH 8.0, total solution volume 2.0 mL.

catalytic activity, but in actuality, this slope is a measure of the initial quantum yield. Under the conditions in Figure 6, the O_2 yields and quantum yields in the presence of $\mathbf{Co_2Ni_2P_2}$ are reproducibly ~23% higher than those of in the presence of $\mathbf{Co_4P_2}$. The O_2 yields in the $\mathbf{Ni_4P_2}$ and $\mathbf{Na_2Ni_2P_2}$ reactions are the same as those without a catalyst. The light-induced oxidative decomposition of the photosensitizer, $[Ru(bpy)_3]^{2+}$, by persulfate is the main side reaction in the absence of a water oxidation catalyst.

Stability of the $Co_2Ni_2P_2$ Water Oxidation Catalyst in Solution. Four different experiments described below quantify the stability of the catalyst under turnover conditions and rule out $[Co(H_2O)_6]^{2+}$ as a significant WOC. All the details, including considerations and controls for each, are in the Supporting Information:

1. $\mathbf{Co_2Ni_2P_2}$ was extracted by tetra-*n*-heptylammonium $(THpA)NO_3$ from the post-reaction solution into toluene. The aqueous layer was evaluated by cathodic adsorptive stripping voltammetry to quantify the amount of Co(II) from POM decomposition. The concentrations of Co(II) in NaBi buffer (100 mM, pH = 8.0) and NaPi buffer (100 mM, pH = 8.0) were 5 and 10%. These concentrations are for too low for the observed catalytic activity of $\mathbf{Co_2Ni_2P_2}$.[71,72]
2. The concentration of Co(II) present in $\mathbf{Co_2Ni_2P_2}$ solutions was also determined by ^{31}P NMR line broadening analysis. We found that the decomposition of 5 μM $\mathbf{Co_2Ni_2P_2}$ to Co(II) after 1 h in 0.1 M NaPi at pH 8.0 did not exceed 14%.[73,74]
3. The dependence of catalytic activity on the storage time of $\mathbf{Co_2Ni_2P_2}$ in stock solution in 160 mM NaBi buffer at pH 8.0 was measured by stopped flow kinetics analysis (Figure S12). After 1 h of storage, the activity of $\mathbf{Co_2Ni_2P_2}$ did not change, again suggesting the significant hydrolytic stability of $\mathbf{Co_2Ni_2P_2}$ in borate buffer at pH 8.0.
4. The addition of bipyridine (bpy) to the solution of Co_{aq}^{2+} results in the formation of mono-, bis, and tris-bpy complexes of Co(II) with $\log_{10}(\beta_i)$ values of 5.65, 11.25, and 16.05.[75] In the solution of 1.0 μM Co^{2+} and 9.0 μM bpy, the concentration of free Co^{2+} is lower than 0.02 μM. The addition of small amounts of bpy to the Co^{2+}-catalyzed water oxidation (H_2O + $[Ru(bpy)_3]^{3+}$) completely shuts down the reaction. If 9.0 μM bpy is added to the reaction catalyzed by 1.0 μM $\mathbf{Co_2Ni_2P_2}$, only a very small decrease of $[Ru(bpy)_3]^{3+}$ consumption is observed (Figure 5). This confirms that Co(II) cannot be the true catalyst in the $\mathbf{Co_2Ni_2P_2}$ solution. However, because the bpy ligand notably destabilizes the $\mathbf{Co_2Ni_2P_2}$ POM framework (removes Co(II)) as it does in the case of $\mathbf{Co_4V_2}$,[74] and unlike in the case of $\mathbf{Co_4P_2}$,[72] the addition of 40 μM bpy results in a visible inhibition of the reaction.

Electrocatalytic Water Oxidation. Previous studies showed that prolonged exposure to the high overpotential conditions required for electrochemical water oxidation tends to decompose cobalt-containing Keggin-sandwich POMs by electrodepositing cobalt oxide species on the working electrode.[71,72,74,76] Embedding Co-POM WOCs in carbon paste has been reported to greatly reduce the hydrolytic decomposition of these catalysts.[40,42] However, short-timescale homogeneous cyclic voltammetry experiments illuminate aspects of the catalytic water oxidation activity of $\mathbf{Co_2Ni_2P_2}$. At 1.0 μM, this POM produces an increasing anodic current from the catalytic oxidation of water with no corresponding reductive current (Figure 7). More importantly, atom equivalent concentrations of aqueous Co^{2+} and Ni^{2+} (2.0 μM each) result in lower oxidative currents. Given that aqueous Co^{2+} is a known active WOC (active WOC precursor) and Ni^{2+} is not, this observation strongly suggests that $\mathbf{Co_2Ni_2P_2}$ is a much faster WOC than Co^{2+}. These results are also consistent with the stopped-flow kinetic studies, where we see not only a much faster initial rate of reaction associated with $\mathbf{Co_2Ni_2P_2}$ but also a delayed reaction onset for aqueous Co^{2+} that is nonexistent in the early-time water oxidations catalyzed by POM WOCs.

With the above control experiments done, we now compare the electrocatalytic activities of $\mathbf{Co_4P_2}$ and $\mathbf{Co_2Ni_2P_2}$ in Figure 8. The onset potential of catalytic water oxidation is lower for $\mathbf{Co_2Ni_2P_2}$ than for $\mathbf{Co_4P_2}$, and the current at a given potential after onset of water oxidation is higher for $\mathbf{Co_2Ni_2P_2}$ than for $\mathbf{Co_4P_2}$. Thus, for all three of the standard modes of WOC

https://doi.org/10.1021/acs.inorgchem.2c00446
Inorg. Chem. 2022, 61, 6252−6262

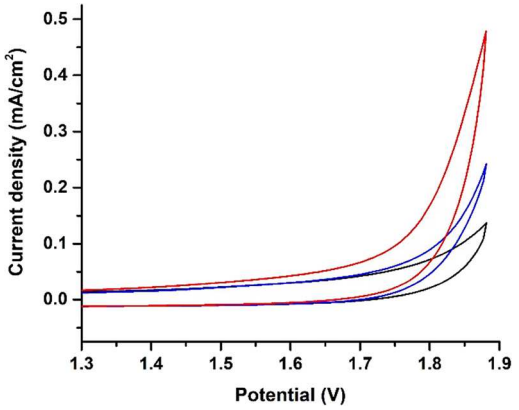

Figure 7. Cyclic voltammetry of different catalytic species. No catalyst (black), 1.0 μM $\mathbf{Co_2Ni_2P_2}$ (red), and 2.0 μM $Co(NO_3)_2$ + 2.0 μM Ni $Co(NO_3)_2$ (blue). Conditions: 0.1 M pH 8.0 borate buffer with 0.1 M KNO_3 as the electrolyte; a planar glassy carbon working electrode with a diameter of 3 mm; a Ag/AgCl reference electrode; 50 mV/s scan rate. The plotted potential is based on the reversible hydrogen electrode.

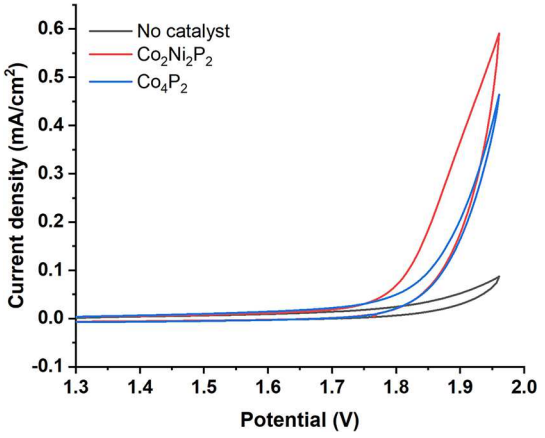

Figure 8. Cyclic voltammograms comparing the electrocatalytic water oxidation current for no catalyst (black), 1.0 μM $\mathbf{Co_2Ni_2P_2}$ (red), and 1.0 μM $\mathbf{Co_4P_2}$ (blue). The electrodes and conditions are identical to those in Figure 7.

assessment, thermal with an oxidant, photo-driven with a photosentizer plus terminal electron acceptor (persulfate), and electrocatalytic, $\mathbf{Co_2Ni_2P_2}$ is more active than $\mathbf{Co_4P_2}$. The most direct measurement of homogeneous WOC rates would be from the dark thermal reactions because, as we have noted, processes other than water oxidation to O_2 are largely rate limiting in photosensitized water oxidation by persulfate, and decomposition of these POM WOCs can be operative during electrocatalytic water oxidation, although our controls indicate that the latter process is not important in the reported experiments here.

Evaluation of Electronic Structures and Mechanisms of Water Oxidation Catalyzed by $\mathbf{Co_2Ni_2P_2}$ and $\mathbf{Co_4P_2}$. In order to explain the order of magnitude higher WOC activity of $\mathbf{Co_2Ni_2P_2}$ compared to $\mathbf{Co_4P_2}$, we studied in detail the kinetics of catalytic $[Ru(bpy)_3]^{3+}$ consumption. First, we attempted to estimate the standard reduction potentials of these POMs. The common electrochemical technique does not work in this case. Neither POMs show any electroactive redox behavior prior to their water oxidation catalytic current. Consequently, we performed potentiometric titration by $[Ru(bpy)_3]^{3+}$ (E = 1.26 V) using a stopped flow technique and measuring the $[Ru(bpy)_3]^{2+}$ concentration at 450 nm (ε = 1.42 × 10^4 M^{-1} cm^{-1}). The stock solution used for titration was a mixture of $[Ru(bpy)_3]^{3+}$ and $[Ru(bpy)_3]^{2+}$ in a 6:1 ratio. The addition of 0.8−3.0 equiv of $[Ru(bpy)_3]^{3+}$ to 50 μM of either $\mathbf{Co_2Ni_2P_2}$ or $\mathbf{Co_4P_2}$ resulted in an immediate (after 0.01 s) increase of absorbance at 450 nm due to the presence of $[Ru(bpy)_3]^{2+}$ in a stock solution. The absorbance grows exponentially with a $k \approx 0.15$ s^{-1}. The rate constant of $[Ru(bpy)_3]^{3+}$ self-decomposition is between 0.02 and 0.025 s^{-1}. Therefore, the self-decomposition cannot be ignored, and as a compromise, we measured the concentration of $[Ru(bpy)_3]^{2+}$ 2.0 s after mixing in the titration procedure. In the presence of 50 μM $\mathbf{Co_2Ni_2P_2}$, the yield of $[Ru(bpy)_3]^{2+}$ formed was about 15−20% of added $[Ru(bpy)_3]^{3+}$ (Figure S13). Correspondingly, the first oxidation potential of $\mathbf{Co_2Ni_2P_2}$ must be 20−40 mV higher than that of $[Ru(bpy)_3]^{3+}$. Similar results, within the experimental error, were obtained for titration of $\mathbf{Co_4P_2}$.

Based on this finding, we constructed a kinetic model for the catalytic reduction of $[Ru(bpy)_3]^{3+}$. We rule out a sequential oxidation of these POMs by four electrons for three reasons: (a) commonly, the oxidation potentials increase with the number of removed electrons, even with redox leveling, (b) both $\mathbf{Co_2Ni_2P_2}$ and $\mathbf{Co_4P_2}$ already have high first Co(III)/Co(II) potentials, and (c) $[Ru(bpy)_3]^{3+}$ is unlikely able to remove three additional electrons sequentially. Therefore, we assume that two molecules of $[Ru(bpy)_3]^{3+}$ oxidize one POM to form a two-electron-oxidized intermediate that then reacts with water. The resulting peroxy-like species is rapidly oxidized subsequently by two $[Ru(bpy)_3]^{3+}$ to form O_2 and regenerate the initial form of the POM. The simplified kinetic model is shown in eqs 4−7:

$$\mathrm{POM} + [Ru(bpy)_3]^{3+} \leftrightarrows \mathrm{POM(1)} + [Ru(bpy)_3]^{2+} \quad \Delta G1 \tag{4}$$

$$\mathrm{POM(1)} + [Ru(bpy)_3]^{3+} \leftrightarrows \mathrm{POM(2)} + [Ru(bpy)_3]^{2+} \quad \Delta G2 \tag{5}$$

$$\mathrm{POM(2)} \rightarrow \mathrm{HO-O-CoPOM} \qquad k_c \tag{6}$$

$$\mathrm{HO-O-CoPOM} + 2[Ru(bpy)_3]^{3+} \rightarrow \mathrm{POM} + 2[Ru(bpy)_3]^{2+} + O_2 \quad \text{fast} \tag{7}$$

where POM(1) and POM(2) are the one- and two-electron oxidized forms of the initial POM catalyst, and HO−O−CoPOM represents the key cobalt−peroxy intermediate in the rate-determining step.

The self-decomposition of $[Ru(bpy)_3]^{3+}$ is a complex process. The decay of absorbance at 670 nm is exponential, but the yield of the $[Ru(bpy)_3]^{2+}$ product is higher than 95% based on the initial $[Ru(bpy)_3]^{3+}$. Bpy self-decomposition in oxidative processes has been thoroughly studied in previous work that shows that the oxidatively damaged bpy ligand, bpy′, which is almost always more electron-rich than bpy itself, is easily oxidized to CO_2.[68] To take into account the stoichiometry of bpy self-decomposition, we add reactions 8 and 9 to the kinetic model:

$$[Ru(bpy)_3]^{3+} \rightarrow [Ru(bpy')(bpy)_2]^{2+} \quad \text{self-decomposition} \tag{8}$$

https://doi.org/10.1021/acs.inorgchem.2c00446
Inorg. Chem. 2022, 61, 6252−6262

Analysis of this model affords the following values (details of the fitting procedure and results are described in the Supporting Information) for $Co_2Ni_2P_2$ (Co_4P_2):

$$\Delta G1 = 29\ (21)\ \text{mV},\ \Delta G2 = -34\ (-33)\ \text{mV},\ k_c = 1.1 \times 10^{+3}\ (20)\ s^{-1} \quad (9)$$

Thus, the main reason for the significant difference in catalytic activity between the two POMs seems to be the difference in rates of eq 6, which includes O−O bond formation. To support this hypothesis, we performed quantum-chemical calculations of thermodynamic properties of the intermediates likely involved in the water oxidation catalyzed by $Co_2Ni_2P_2$ and Co_4P_2. The details are described in the Supporting Information. The simplified energy diagram is presented in Figure 9. Accordingly,

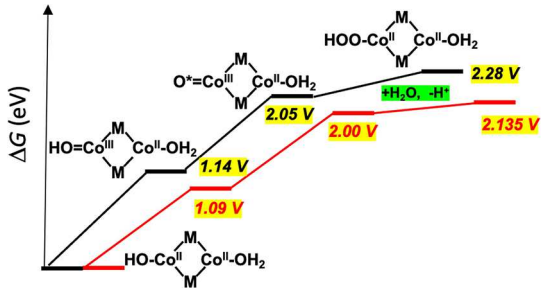

Figure 9. Calculated thermodynamics of the CoO−OH hydroperoxo and other intermediates that form with $Co_2Ni_2P_2$ (M = Ni, red) and Co_4P_2 (M = Co, black), shown in a single reaction pathway for both Co_4P_2 and $Co_2Ni_2P_2$ complexes.

the difference in activity between these POMs derives primarily from the more favorable thermodynamics of the peroxo (O−O)-forming step for $Co_2Ni_2P_2$ than for Co_4P_2. This is analogous to the rate-determining step proposed in other 3d-metal-oxide-based oxidations.[77−79] Specifically, the second-order interaction energy of a bonding Co−O orbital with an adjacent Co d-orbital lone-pair is ∼0.5 kcal/mol in Co_4P_2, while the same interaction of a bonding Co−O orbital with an adjacent Ni d-orbital lone-pair is ∼1.7 kcal/mol in $Co_2Ni_2P_2$. This subtle perturbative interaction acts to stabilize the peroxo formation free-energy reaction path for $Co_2Ni_2P_2$ by about 1.1 kcal/mol at the transition state and about 1.6 kcal/mol in the peroxo product. These energy differences are significant at 300 K. Thus, based on the above electronic structure calculations, we believe that the indirect inner-metal−outer-metal interaction energies explains, at least in part, the observed difference in the reaction rates between $Co_2Ni_2P_2$ and Co_4P_2. The reaction pathway and an orbital interaction energy diagram are presented in Figure S17.

CONCLUSIONS

This study demonstrates that multiwavelength synchrotron X-radiation anomalous dispersion scattering (synchrotron XRAS) can address a pervasive challenge with metal oxide and POM water oxidation catalysts (WOCs) containing two 3d metals: confirming the positions of both the catalytic active site metal and the second potentially non-innocent adjacent metal. Knowing both the location and percent occupancies of the two 3d metals is fundamental to reactivity, stability, spectroscopic, and other properties of such catalysts and studies thereof. Conventional single-wavelength X-ray crystallographic determination cannot unequivocally distinguish two adjacent 3d elements because of very similar electron densities. In this study, we also report a high-yield, site-selective synthesis of a sandwich POM WOC with two different 3d metals, $Co_2Ni_2P_2$, which is isostructural and bears the same charge (10−) as the parent tetra-cobalt WOC studied by several groups, Co_4P_2 (X-ray structures of both in Figure 1). The use of XRAS, with data collection and refinements over many wavelengths, proves that Co centers and Ni centers in $Co_2Ni_2P_2$ reside essentially only on the outside and inside positions of the central belt, respectively, facilitating a quantitative comparison of the properties of $Co_2Ni_2P_2$ and Co_4P_2, the first such study in any WOC.

$Co_2Ni_2P_2$ is an order of magnitude faster as a water oxidation catalyst than Co_4P_2. Additional experimental studies show different spectroscopic and electrochemical properties of the two POM catalysts, while experimental and computational data reveal major differences in the electronic structures of $Co_2Ni_2P_2$ versus Co_4P_2 upon changing the inside active-site-adjacent 3d metal: Co in Co_4P_2 versus Ni in $Co_2Ni_2P_2$.

Four independent experiments establish that these POMs are the active water oxidation species under catalytic conditions. Aqueous Co^{2+} is not catalytically important.

Multiwavelength XRAS should be definitive for structural assignments in myriad potential multiple-transition-metal-containing catalysts including but not limited to those central to solar fuel production: HER, OER (WO), and carbon dioxide reduction (CO_2RR) catalysts.

METHODS AND MATERIALS (SEE THE SUPPORTING INFORMATION FOR FULL EXPERIMENTAL DETAILS)

Co(II) in Buffered Catalytic Solutions. By convention, Co(II) in aqueous solution is denoted as "Co^{2+}" or "$[Co(H_2O)_6]^{2+}$"; however, divalent cobalt in the borate and phosphate buffers used to control pH in the catalysis and stability studies in this paper replace some of aqua ligands bound to cobalt, and thus writing "$[Co(H_2O)_6]^{2+}$" in the buffered solution studies is somewhat misleading. As a consequence, we write divalent cobalt in this paper as "Co(II)" for these studies that encompasses the different hydrolysis and association species of cobalt. The Co(II)-buffer association equilibria are discussed and where possible quantified in the Supporting Information (SI).[80,81] In contrast, writing "$[Co(H_2O)_6]^{2+}$" is appropriate for the syntheses and X-ray crystallographic studies where all six aqua ligands of the cobalt counterions are confirmed.

Synthesis of $K_8Na_4[Na_2Ni_2(PW_9O_{34})_2]\cdot 30H_2O$ ($Na_2Ni_2P_2$).[63] $Na_2WO_4\cdot 2H_2O$ (5 g, 15.2 mmol) and Na_2HPO_4 (0.24 g, 1.7 mmol) were dissolved in 50 mL of H_2O followed by the addition of $Ni(NO_3)_2\cdot 6H_2O$ (0.32 g, 1.1 mmol), resulting in a cloudy suspension. The pH was adjusted to 7.5 by dropwise addition of 6 M HCl, and a yellow-green solution formed. The solution was heated at 90 °C for 1 h and then was allowed to cool to room temperature. Powdered KCl (0.6 g, 8.0 mmol) was added, and the solution was allowed to evaporate for several days at room temperature generating 0.2 g of yellow-green needles (7% yield based on W).

Synthesis of $K_{10}[Co_2Ni_2(PW_9O_{34})_2]\cdot 28H_2O$ ($K_{10}Co_2Ni_2P_2$) $Na_2Ni_2P_2$. $Na_2Ni_2P_2$ (0.04 g) was dissolved in 4 mL of 1 M $CoCl_2$ aqueous solution. KCl (0.08 g in 1 mL of solution) was added under stirring at 50 °C to accelerate the crystallization. Dark purple-brown crystals with two $[Co(H_2O)_6]^{2+}$ as counterions to the deca-anion, $Co_2Ni_2P_2$, were obtained overnight upon slow evaporation (0.028 g, 70% yield). The two $[Co(H_2O)_6]^{2+}$ counterions were quantitatively removed by recrystallization as follows: 5 mg of the above crystals were dissolved in 4 mL of water, and 1 mL of KCl solution (0.1 g·mL^{-1}) was added under stirring at 50 °C. Single crystals suitable for X-ray crystallography were obtained overnight upon slow evaporation (yield 2.5 mg, 50%). FTIR data (cm^{-1}): 1039(s), 1012(s), 936(sh), 889(sh), 700(s). The TGA measurement indicated 30 water molecules of crystallization. Elemental analysis calcd (wt %) for $Co_2Ni_2P_2$: Co, 2.22;

https://doi.org/10.1021/acs.inorgchem.2c00446
Inorg. Chem. 2022, 61, 6252−6262

Ni, 2.21; P, 1.15; W, 62.46; found (wt %): Co, 2.00; Ni, 2.11; P, 1.04; W, 61.70.

The POMs, $Na_{10}[Co_4(H_2O)_2(PW_9O_{34})_2]\cdot 27H_2O$ ($\mathbf{Co_4P_2}$) and $Na_6K_4[Ni_4(H_2O)_2(PW_9O_{34})_2]\cdot 32H_2O$ ($\mathbf{Ni_4P_2}$), for control experiments were synthesized by the literature procedures.[30,82]

X-ray Structure of the POMs. These routine determinations are described in the Supporting Information and in the available CIF files.

XRAS Experiments. Standard, single-wavelength X-ray diffraction is generally not sensitive enough to unequivocally distinguish neighboring transition-metal atoms in the periodic table in a molecule. This is particularly true where there are many adjacent heavy atoms, as in the case of $\mathbf{Co_2Ni_2P_2}$ that contains 18 tungsten atoms. Synchrotron XRAS proved to be ideal for this purpose. Key aspects of the technique pertaining to $\mathbf{Co_2Ni_2P_2}$ are in the Results and Discussion, and the technical basics and scattering details are given in the Supporting Information. Six data sets were collected at the Advanced Photon Source (15-ID-B) using radiation close to the K-edges of cobalt and nickel to unequivocally determine the exact nature of these metal atoms in the central belt of $\mathbf{Co_2Ni_2P_2}$. Specifically, measurements were performed and displaced at either side of the K-edges of Co (1.608 Å, 7.71 keV) and Ni (1.488 Å, 8.33 keV). The conditions available at 15-ID-B enabled collection of extremely high-resolution, multi-wavelength, and complete data sets that are responsive to the exact composition of the Co/Ni atom sites in the crystal.

Evaluation of Catalytic Activity. The catalytic activity toward water oxidation was evaluated using the techniques described earlier[31,69] and also addressed above. The O_2 yield in water oxidation by $[Ru(bpy)_3]^{3+}$ was measured in a custom-built apparatus that was described in detail earlier.[83] The oxygen concentration was measured by an Ocean Optics Neofox Phase Measurement System containing a calibrated FOXY-R probe with a FOXY-AFMG coating. The measurements were performed until the oxygen reading was constant for 3−5 consecutive experiments. Analysis of oxygen in the reaction headspace in the light-driven system was performed using a HP7890A model gas chromatograph (GC) equipped with a thermal conductivity detector (TCD) and a 5 Å molecular sieve capillary column. The kinetics and the O_2 yields in this system are strongly dependent on the stirring rate, light intensity, and configuration of a light source and a reactor.[31,72] Therefore, this technique is applicable only for determining the relative catalytic activities of different complexes under strictly identical conditions.

Computational Details. Here, we used the M06L density functional[84] in conjuction with the 6-31G(d,p) basis sets for P, O, and H atoms and LANL2DZ ECPs with the corresponding basis sets for W, Co, and Ni. The effects of bulk aqueous solution were approximated at the level of the polarizable continuum model (PCM).[85] Roles of the long-range dispersion interactions were evaluated using the GD3 method.[86] Geometry optimizations of all structures were done without symmetry constraints and at their energetically lowest high-spin states. All the calculations were performed using the Gaussian 09 (Revision E.01) quantum chemical software package[87] (for more details, see the Supporting Information).

■ ASSOCIATED CONTENT

Supporting Information

The Supporting Information is available free of charge at https://pubs.acs.org/doi/10.1021/acs.inorgchem.2c00446.

Experimental details, materials, methods, and additional supporting figures as described in the text (PDF)

Accession Codes

CCDC 2089909 and 2089937 contain the supplementary crystallographic data for this paper. These data can be obtained free of charge via www.ccdc.cam.ac.uk/data_request/cif, or by emailing data_request@ccdc.cam.ac.uk, or by contacting The Cambridge Crystallographic Data Centre, 12 Union Road, Cambridge CB2 1EZ, UK; fax: +44 1223 336033.

■ AUTHOR INFORMATION

Corresponding Author

Craig L. Hill − *Department of Chemistry, Emory University, Atlanta, Georgia 30322, United States;* orcid.org/0000-0002-5506-9588; Email: chill@emory.edu

Authors

Meilin Tao − *Department of Chemistry, Emory University, Atlanta, Georgia 30322, United States*

Qiushi Yin − *Department of Chemistry, Emory University, Atlanta, Georgia 30322, United States*

Alexey L. Kaledin − *Emerson Center for Scientific Computation, Emory University, Atlanta, Georgia 30322, United States;* orcid.org/0000-0003-3112-3989

Natalie Uhlikova − *Department of Chemistry, Emory University, Atlanta, Georgia 30322, United States*

Xinlin Lu − *Department of Chemistry, Emory University, Atlanta, Georgia 30322, United States*

Ting Cheng − *Department of Chemistry, Emory University, Atlanta, Georgia 30322, United States*

Yu-Sheng Chen − *ChemMatCARS/The University of Chicago, Lemont, Illinois 60439, United States*

Tianquan Lian − *Department of Chemistry, Emory University, Atlanta, Georgia 30322, United States;* orcid.org/0000-0002-8351-3690

Yurii V. Geletii − *Department of Chemistry, Emory University, Atlanta, Georgia 30322, United States;* orcid.org/0000-0002-2287-330X

Djamaladdin G. Musaev − *Department of Chemistry and Emerson Center for Scientific Computation, Emory University, Atlanta, Georgia 30322, United States;* orcid.org/0000-0003-1160-6131

John Bacsa − *Department of Chemistry, Emory University, Atlanta, Georgia 30322, United States*

Complete contact information is available at: https://pubs.acs.org/10.1021/acs.inorgchem.2c00446

Author Contributions

‖M.T. and Q.Y. contributed equally to the work.

Author Contributions

The authors have given approval to the final version of the manuscript.

Notes

The authors declare no competing financial interest.

■ ACKNOWLEDGMENTS

This work was supported by the US Department of Energy, Office of Basic Energy Sciences, Solar Photochemistry Program (DE-FG02-07ER15906) to C.L.H., T.L., and D.G.M. The authors gratefully acknowledge the resources of the Cherry Emerson Center for Scientific Computation−NSF MRI-R2 grant (CHE-0958205). NSF's ChemMatCARS Sector 15 is supported by the Divisions of Chemistry (CHE) and Materials Research (DMR), National Science Foundation, under grant number NSF/CHE-1834750. Use of the Advanced Photon Source, an Office of Science User Facility operated for the U.S. Department of Energy (DOE) Office of Science by Argonne National Laboratory, was supported by the U.S. DOE under Contract No. DE-AC02-06CH11357.

REFERENCES

(1) Concepcion, J. J.; Jurss, J. W.; Brennaman, M. K.; Hoertz, P. G.; Patrocinio, A. O. T.; Iha, N. Y. M.; Templeton, J. L.; Meyer, T. J. Making Oxygen with Ruthenium Complexes. *Acc. Chem. Res.* **2009**, *42*, 1954−1965.

(2) Eisenberg, R.; Gray, H. B. Preface on Making Oxygen. *Inorg. Chem.* **2008**, *47*, 1697−1699.

(3) Eisenberg, R. Rethinking Water Splitting. *Science* **2009**, *324*, 44−45.

(4) Kärkäs, M. D.; Verho, O.; Johnston, E. V.; Åkermark, B. Artificial Photosynthesis: Molecular Systems for Catalytic Water Oxidation. *Chem. Rev.* **2014**, *114*, 11863−12001.

(5) Blakemore, J. D.; Crabtree, R. H.; Brudvig, G. W. Molecular Catalysts for Water Oxidation. *Chem. Rev.* **2015**, *115*, 12974−13005.

(6) McCrory, C. C. L.; Jung, S.; Ferrer, I. M.; Chatman, S. M.; Peters, J. C.; Jaramillo, T. F. Benchmarking Hydrogen Evolving Reaction and Oxygen Evolving Reaction Electrocatalysts for Solar Water Splitting Devices. *J. Am. Chem. Soc.* **2015**, *137*, 4347−4357.

(7) Lauinger, S. M.; Yin, Q.; Geletii, Y. V.; Hill, C. L., Polyoxometalate Multielectron Catalysts in Solar Fuel Production. In *Advances in Inorganic Chemistry. Polyoxometallate Chemistry*, Volume *69*, 1st ed.; Cronin, L.; Eldik, R. v., Eds. Elsevier: Oxford, UK 2017; pp. 117−154.

(8) Li, J.; Güttinger, R.; Moré, R.; Song, F.; Wan, W.; Patzke, G. R. Frontiers of water oxidation: the quest for true catalysts. *Chem. Soc. Rev.* **2017**, *46*, 6124−6147.

(9) Mondschein, J. S.; Callejas, J. F.; Read, C. G.; Chen, J. Y. C.; Holder, C. F.; Badding, C. K.; Schaak, R. E. Crystalline Cobalt Oxide Films for Sustained Electrocatalytic Oxygen Evolution under Strongly Acidic Conditions. *Chem. Mater.* **2016**, *29*, 950−957.

(10) Lyons, M. E. G.; Doyle, R. L.; Browne, M. P.; Godwin, I. J.; Rovetta, A. A. S. Recent developments in electrochemical water oxidation. *Curr. Opin. Electrochem.* **2017**, *1*, 40−45.

(11) Song, F.; Busch, M. M.; Lassalle-Kaiser, B.; Hsu, C.-S.; Petkucheva, E.; Bensimon, M.; Chen, H. M.; Corminboeuf, C.; Hu, X. An Unconventional Iron Nickel Catalyst for the Oxygen Evolution Reaction. *ACS Cent. Sci.* **2019**, *5*, 558−568.

(12) Matheu, R.; Garrido-Barros, P.; Gil-Sepulcre, M.; Ertem, M. Z.; Sala, X.; Gimbert-Suriñach, C.; Llobet, A. The development of molecular water oxidation catalysts. *Nat. Rev. Chem.* **2019**, *3*, 331−341.

(13) Hunter, B. M.; Gray, H. B.; Müller, A. M. Earth-Abundant Heterogeneous Water Oxidation Catalysts. *Chem. Rev.* **2016**, *116*, 14120−14136.

(14) Niu, F.; Wang, D.; Li, F.; Liu, Y.; Shen, S.; Meyer, T. J. Hybrid Photoelectrochemical Water Splitting Systems: From Interface Design to System Assembly. *Adv. Energy Mater.* **2020**, *10*, 24.

(15) Zhang, B.; Sun, L. Artificial photosynthesis: opportunities and challenges of molecular catalysts. *Chem. Soc. Rev.* **2019**, *48*, 2216−2264.

(16) Burke, M. S.; Kast, M. G.; Trotochaud, L.; Smith, A. M.; Boettcher, S. W. Cobalt-Iron (Oxy)hydroxide Oxygen Evolution Electrocatalysts: The Role of Structure and Composition on Activity, Stability, and Mechanism. *J. Am. Chem. Soc.* **2015**, *137*, 3638−3648.

(17) Du, P.; Eisenberg, R. Catalysts made of earth-abundant elements (Co, Ni, Fe) for water splitting: Recent progress and future challenges. *Energy Environ. Sci.* **2012**, *5*, 6012−6021.

(18) Enman, L. J.; Stevens, M. B.; Dahan, M. H.; Nellist, M. R.; Toroker, M. C.; Boettcher, S. W. Operando X-Ray Absorption Spectroscopy Shows Iron Oxidation Is Concurrent with Oxygen Evolution in Cobalt−Iron (Oxy)hydroxide Electrocatalysts. *Angew. Chem., Int. Ed.* **2018**, *57*, 12840−12844.

(19) Fan, J.; Chen, Z.; Shi, H.; Zhao, G. In situ grown, self-supported iron−cobalt−nickel alloy amorphous oxide nanosheets with low overpotential toward water oxidation. *Chem. Commun.* **2016**, *52*, 4290−4293.

(20) Gerken, J. B.; Landis, E. C.; Hamers, R. J.; Stahl, S. S. Fluoride-Modulated Cobalt Catalysts for Electrochemical Oxidation of Water under Non-Alkaline Conditions. *ChemSusChem* **2010**, *3*, 1176−1179.

(21) Ndambakuwa, W.; Ndambakuwa, Y.; Choi, J.; Fernando, G.; Neupane, D.; Mishra, S. R.; Perez, F.; Gupta, R. K. Nanostructured nickel-cobalt oxide and sulfide for applications in supercapacitors and green energy production using waste water. *Surf. Coat. Technol.* **2021**, *410*, 10.

(22) Peng, Z.; Jia, D.; Al-Enizi, A. M.; Elzatahry, A. A.; Zheng, G. From Water Oxidation to Reduction: Homologous Ni−Co Based Nanowires as Complementary Water Splitting Electrocatalysts. *Adv. Energy Mater.* **2015**, *5*, 1402031.

(23) Smith, R. D. L.; Prévot, M. S.; Fagan, R. D.; Trudel, S.; Berlinguette, C. P. Water Oxidation Catalysis: Electrocatalytic Response to Metal Stoichiometry in Amorphous Metal Oxide Films Containing Iron, Cobalt, and Nickel. *J. Am. Chem. Soc.* **2013**, *135*, 11580−11586.

(24) Wang, Y.; Yang, C.; Huang, Y.; Li, Z.; Liang, Z.; Cao, G. Nickel induced electronic structural regulation of cobalt hydroxide for enhanced water oxidation. *J. Mater. Chem. A* **2020**, *8*, 6699−6708.

(25) Xu, Y. F.; Gao, M. R.; Zheng, Y. R.; Jiang, J.; Yu, S. H. Nickel/Nickel(II) Oxide Nanoparticles Anchored onto Cobalt(IV) Diselenide Nanobelts for the Electrochemical Production of Hydrogen. *Angew. Chem., Int. Ed.* **2013**, *52*, 8546−8550.

(26) Zhu, C.; Wen, D.; Leubner, S.; Oschatz, M.; Liu, W.; Holzschuh, M.; Simon, F.; Kaskel, S.; Eychmüller, A. Nickel cobalt oxide hollow nanosponges as advanced electrocatalysts for the oxygen evolution reaction. *Chem. Commun.* **2015**, *51*, 7851−7854.

(27) Geletii, Y. V.; Botar, B.; Kögerler, P.; Hillesheim, D. A.; Musaev, D. G.; Hill, C. L. An All-Inorganic, Stable, and Highly Active Tetraruthenium Homogeneous Catalyst for Water Oxidation. Selected as the VIP Article by the reviewers and editor. *Angew. Chem., Int. Ed.* **2008**, *47*, 3896−3899.

(28) Sartorel, A.; Carraro, M.; Scorrano, G.; Zorzi, R. D.; Geremia, S.; McDaniel, N. D.; Bernhard, S.; Bonchio, M. Polyoxometalate Embedding of a Tetraruthenium(IV)-oxo-core by Template-Directed Metalation of $[\gamma\text{-}SiW_{10}O_{36}]^{8-}$: A Totally Inorganic Oxygen-Evolving Catalyst. *J. Am. Chem. Soc.* **2008**, *130*, 5006−5007.

(29) Geletii, Y. V.; Besson, C.; Hou, Y.; Yin, Q.; Musaev, D. G.; Quiñonero, D.; Cao, R.; Hardcastle, K. I.; Proust, A.; Kögerler, P.; Hill, C. L. Structural, Physicochemical and Reactivity Properties of an All-Inorganic, Highly Active Tetraruthenium Homogeneous Catalyst for Water Oxidation. *J. Am. Chem. Soc.* **2009**, *131*, 17360−17370.

(30) Yin, Q.; Tan, J. M.; Besson, C.; Geletii, Y. V.; Musaev, D. G.; Kuznetsov, A. E.; Luo, Z.; Hardcastle, K. I.; Hill, C. L. A fast soluble carbon-free molecular water oxidation catalyst based on abundant metals. *Science* **2010**, *328*, 342−345.

(31) Huang, Z.; Luo, Z.; Geletii, Y. V.; Vickers, J. W.; Yin, Q.; Wu, D.; Hou, Y.; Ding, Y.; Song, J.; Musaev, D. G.; Hill, C. L.; Lian, T. Efficient Light-Driven Carbon-Free Cobalt-Based Molecular Catalyst for Water Oxidation. *J. Am. Chem. Soc.* **2011**, *133*, 2068−2071.

(32) Toma, F. M.; Sartorel, A.; Iurlo, M.; Carraro, M.; Parisse, P.; Maccato, C.; Rapino, S.; Gonzalez, B. R.; Amenitsch, H.; Da Ros, T.; Casalis, L.; Goldoni, A.; Marcaccio, M.; Scorrano, G.; Scoles, G.; Paolucci, F.; Prato, M.; Bonchio, M. Efficient Water Oxidation at Carbon Nanotube−Polyoxometalate Electrocatalytic Interfaces. *Nat. Chem.* **2010**, *2*, 826−831.

(33) Carraro, M.; Sartorel, A.; Toma, F. M.; Puntoriero, F.; Scandola, F.; Campagna, S.; Prato, M.; Bonchio, M. Artificial Photosynthesis Challenges: Water Oxidation at Nanostructured Interfaces. *Top. Curr. Chem.* **2011**, *303*, 121−150.

(34) Car, P.-E.; Guttentag, M.; Baldridge, K. K.; Alberto, R.; Patzke, G. R. Synthesis and characterization of open and sandwich-type polyoxometalates reveals visible-light-driven water oxidation *via* POM-photosensitizer complexes. *Green Chem.* **2012**, *14*, 1680−1688.

(35) Mukhopadhyay, S.; Debgupta, J.; Singh, C.; Kar, A.; Das, S. K. A Keggin Polyoxometalate Shows Water Oxidation Activity at Neutral pH: POM@ZIF-8, an Efficient and Robust Electrocatalyst. *Angew. Chem., Int. Ed.* **2018**, *57*, 1918−1923.

(36) Liu, B.; Glass, E. N.; Wang, R.-P.; Cui, Y.-T.; Harada, Y.; Huang, D.-J.; Schuppler, S.; Hill, C. L.; de Groot, F. M. F. Cobalt-to-vanadium charge transfer in polyoxometalate water oxidation catalysts revealed by 2p3d resonant inelastic X-ray scattering. *Phys. Chem. Chem. Phys.* **2018**, *20*, 4554−4562.

https://doi.org/10.1021/acs.inorgchem.2c00446
Inorg. Chem. 2022, 61, 6252−6262

(37) Martin-Sabi, M.; Soriano-López, J.; Winter, R. S.; Chen, J.-J.; Vilà-Nadal, L.; Long, D.-L.; Galán-Mascarós, J. R.; Cronin, L. Redox tuning the Weakley-type polyoxometalate archetype for the oxygen evolution reaction. *Nat. Catal.* **2018**, *1*, 208−213.
(38) Han, X.-B.; Zhang, Z.-M.; Zhang, T.; Li, Y.-G.; Lin, W.; You, W.; Su, Z.-M.; Wang, E.-B. Polyoxometalate-Based Cobalt-Phosphate Molecular Catalysts for Visible Light-Driven Water Oxidation. *J. Am. Chem. Soc.* **2014**, *136*, 5359−5366.
(39) Folkman, S. J.; Soriano-Lopez, J.; Galán-Mascarós, J. R.; Finke, R. G. Electrochemically Driven Water-Oxidation Catalysis Beginning with Six Exemplary Cobalt Polyoxometalates: Is It Molecular, Homogeneous Catalysis or Electrode-Bound, Heterogeneous CoO_x Catalysis? *J. Am. Chem. Soc.* **2018**, *140*, 12040−12055.
(40) Blasco-Ahicart, M.; Soriano-López, J.; Carbó, J. J.; Poblet, J. M.; Galan-Mascaros, J. R. Polyoxometalate electrocatalysts based on earth-abundant metals for efficient water oxidation in acidic media. *Nat. Chem.* **2018**, *10*, 24−30.
(41) Haider, A.; Bassil, B. S.; Soriano-López, J.; Qasim, H. M.; de Pipaón, C. S.; Ibrahim, M.; Dutta, D.; Koo, Y.-S.; Carbó, J. J.; Poblet, J. M.; Galán-Mascarós, J. R.; Kortz, U. 9-Cobalt(II)-Containing 27-Tungsto-3-germanate(IV): Synthesis,Structure, Computational Modeling, and Heterogeneous Water Oxidation Catalysis. *Inorg. Chem.* **2019**, *58*, 11308−11316.
(42) Arens, J. T.; Blasco-Ahicart, M.; Azmani, K.; Soriano-López, J.; García-Eguizábal, A.; Poblet, J. M.; Galan-Mascaros, J. R. Water oxidation electrocatalysis in acidic media with Co-containing polyoxometalates. *J. Catal.* **2020**, *389*, 345−351.
(43) Das, S.; Misra, A.; Roy, S. Enhancement of photochemical heterogeneous water oxidation by a manganese based soft oxometalate immobilized on a graphene oxide matrix. *New J. Chem.* **2016**, *40*, 994−1003.
(44) Okuhara, T.; Mizuno, N.; Misono, M. Catalytic Chemistry of Heteropoly Compounds. *Adv. Catal.* **1996**, *41*, 113−252.
(45) Hill, C. L. Introduction: Polyoxometalates—Multicomponent Molecular Vehicles To Probe Fundamental Issues and Practical Problems. *Chem. Rev.* **1998**, *98*, 1−2.
(46) Borrás-Almenar, J. J.; Coronado, E.; Müller, A.; Pope, M. T., *Polyoxometalate Molecular Science. Proceedings of the NATO Advanced Study Institute, Tenerife, Spain from 25 August to 2003*. Kluwer Academic Publishers: Dordrecht, 2003; Vol. *98*, p 484.
(47) Long, D.-L.; Tsunashima, R.; Cronin, L. Polyoxometalates: Building Blocks for Functional Nanoscale Systems. *Angew. Chem., Int. Ed.* **2010**, *49*, 1736−1758.
(48) Badiei, Y. M.; Polyansky, D. E.; Muckerman, J. T.; Szalda, D. J.; Haberdar, R.; Zong, R.; Thummel, R. P.; Fujita, E. Water Oxidation with Mononuclear Ruthenium(II) Polypyridine Complexes Involving a Direct Ru^{IV}=O Pathway in Neutral and Alkaline Media. *Inorg. Chem.* **2013**, *52*, 8845−8850.
(49) Lebedev, D.; Pineda-Galvan, Y.; Tokimaru, Y.; Fedorov, A.; Kaeffer, N.; Copéret, C.; Pushkar, Y. The Key Ru^{V}=O Intermediate of Site-Isolated Mononuclear Water Oxidation Catalyst Detected by *in Situ* X-ray Absorption Spectroscopy. *J. Am. Chem. Soc.* **2018**, *140*, 451−458.
(50) Schiwon, R.; Klingan, K.; Dau, H.; Limberg, C. Shining light on integrity of a tetracobalt-polyoxometalate water oxidation catalyst by X-ray spectroscopy before and after catalysis. *Chem. Commun.* **2014**, *50*, 100−102.
(51) Smith, R. D. L.; Prévot, M. S.; Fagan, R. D.; Zhang, Z.; Sedach, P. A.; Siu, M. K. J.; Trudel, S.; Berlinguette, C. P. Photochemical Route for Accessing Amorphous Metal Oxide Materials for Water Oxidation Catalysis. *Science* **2013**, *340*, 60−63.
(52) Trotochaud, L.; Boettcher, S. W. Precise Oxygen Evolution Catalysts: Status and Opportunities. *Scr. Mater.* **2014**, *74*, 25−32.
(53) Collman, J. P.; Boulatov, R. Heterodinuclear transition-metal complexes with multiple metal-metal bonds. *Angew. Chem., Int. Ed.* **2002**, *41*, 3948−3961.
(54) Guan, W.; Yamabe, S.; Sakaki, S. Interest in new heterodinuclear transition-metal/main-group-metal complexes: DFT study of electronic structure and mechanism of fluoride sensing function. *Dalton Trans.* **2013**, *42*, 8717−8728.
(55) Coombs, J.; Perry, D.; Kwon, D.-H.; Thomas, C. M.; Ess, D. H. Why Two Metals Are Better Than One for Heterodinuclear Cobalt−Zirconium-Catalyzed Kumada Coupling. *Organometallics* **2018**, *37*, 4195−4203.
(56) Gade, L. H.; Memmler, H.; Kauper, U.; Schneider, A.; Fabre, S.; Bezougli, I.; Lutz, M.; Galka, C.; Scowen, I. J.; McPartlin, M. Cooperative Reactivity of Early-Late Heterodinuclear Transition Metal Complexes with Polar Organic Substrates. *Chem. − Eur. J.* **2000**, *6*, 692−708.
(57) Zhang, Y.-P.; Li, Y.; Xu, G.-C.; Li, J.-Y.; Luo, H.-Y.; Li, J.-Y.; Zhang, L.; Jia, D.-Z. Synthesis, crystal structure, DNA/bovine serum albumin binding and antitumor activity of two transition metal complexes with 4-acylpyrazolone derivative. *Appl. Organomet. Chem.* **2019**, *33*, 1099−0739.
(58) Koessler, K.; Butschke, B. Heterodinuclear Transition-Metal Complexes: Fundamentals, Synthesis, and Applications. *Encycl. Inorg. Bioinorg. Chem.* **2021**, 1.
(59) Hong, Z.; Zheng-He, P.; Zhi-Quan, P.; Bo, L.; Xue-Lei, H.; Yong-Qiong, L. Novel heterodinuclear transition metal macrocyclic complexes: syntheses, characterization and crystal structures. *J. Coord. Chem.* **2005**, *58*, 443−451.
(60) Tasiopoulos, A. J.; Milligan, P. L., Jr.; Abboud, K. A.; O'Brien, T. A.; Christou, G. Mixed Transition Metal−Lanthanide Complexes at High Oxidation States: Heteronuclear $Ce^{IV}Mn^{IV}$ Clusters. *Inorg. Chem.* **2007**, *46*, 9678−9691.
(61) Menard, L. D.; Wang, Q.; Kang, J. H.; Sealey, A. J.; Girolami, G. S.; Teng, X.; Frenkel, A. I.; Nuzzo, R. G. Structural characterization of bimetallic nanomaterials with overlapping x-ray absorption edges. *Phys. Rev. B* **2009**, *80*, No. 064111.
(62) Frenkel, A. I. Applications of Extended X-Ray Absorption Fine Structure spectroscopy to studies of bimetallic nanoparticle catalysts. *Chem. Soc. Rev.* **2012**, *41*, 8163−8178.
(63) Hou, Y.; Xu, L.; Cichon, M. J.; Lense, S.; Hardcastle, K. I.; Hill, C. L. A New Family of Sandwich-Type Polytungstophosphates Containing Two Types of Metals in the Central Belt: $M'_2M_2(PW_9O_{34})_2^{12-}$ (M' = Na or Li, M = Mn^{2+}, Co^{2+}, Ni^{2+},and Zn^{2+}). *Inorg. Chem.* **2010**, *49*, 4125−4132.
(64) Doungmene, F.; Aparicio, P. A.; Ntienoue, J.; Ayingone Mezui, C. S.; de Oliveira, P.; López, X.; Mbomekallé, I. M. Electrochemical behaviour of mixed d metal-iron containing Wells-Dawson sandwich-type complexes: $[(FeOH_2)_2M_2(X_2W_{15}O_{56})_2]^{n-}$ and $[(MOH_2)_2Fe_2(X_2W_{15}O_{56})_2]^{n-}$ (M = Cr^{III}, Mn^{III}, Mn^{II}, Co^{II}, Ni^{II}, Cu^{II}, Zn^{II}, X = As^{V} or P^{V} and *n* = 12 or 14). *Electrochem. Acta* **2014**, *125*, 674−682.
(65) Ayingone Mezui, C. S.; de Oliveira, P.; Teillout, A.-L.; Marrot, J.; Berthet, P.; Lebrini, M.; Mbomekallé, I. M. Synthesis, Structure, and Magnetic Electrochemical Properties of a Family of Tungstoarsenates Containing Just Co^{II} Centers or Both Co^{II} and Fe^{III} Centers. *Inorg. Chem.* **2017**, *56*, 1999−2012.
(66) Weakley, T. J. R.; Evans, H. T., Jr.; Showell, J. S.; Tourné, G. F.; Tourné, C. M. 18-Tungstotetracobalto(II)diphosphate and related Anions: a Novel Structural Class of Heteropolyanions. *J. Chem. Soc., Chem. Commun.* **1973**, *4*, 139−140.
(67) Toby, B. H.; Von Dreele, R. B. GSAS-II: the genesis of a modern open-source all purpose crystallography software package. *J. Appl. Crystallography* **2013**, *46*, 544−549.
(68) Ghosh, P. K.; Brunschwig, B. S.; Chou, M.; Creutz, C.; Sutin, N. Thermal and Light-Induced Reduction of $Ru(bpy)_3^{3+}$ in Aqueous Solution. *J. Am. Chem. Soc.* **1984**, *106*, 4772−4783.
(69) Geletii, Y. V.; Huang, Z.; Hou, Y.; Musaev, D. G.; Lian, T.; Hill, C. L. Homogeneous Light-Driven Water Oxidation Catalyzed by a Tetraruthenium Complex with All Inorganic Ligands. *J. Am. Chem. Soc.* **2009**, *131*, 7522−7523.
(70) White, H. S.; Becker, W. G.; Bard, A. J. Photochemistry of the Tris(2,2′-bipyridine)ruthenium(II)-Peroxydisulfate System in Aqueous and Mixed Acetonitrile-Water Solutions. Evidence for a Long-Lived Photoexcited Ion Pair. *J. Phys. Chem.* **1984**, *88*, 1840−1846.

https://doi.org/10.1021/acs.inorgchem.2c00446
Inorg. Chem. 2022, 61, 6252−6262

(71) Stracke, J. J.; Finke, R. G. Electrocatalytic Water Oxidation Beginning with the Cobalt Polyoxometalate $[Co_4(H_2O)_2(PW_9O_{34})_2]^{10-}$: Identification of Heterogeneous CoO_x as the Dominant Catalyst. *J. Am. Chem. Soc.* **2011**, *133*, 14872−14875.
(72) Vickers, J. W.; Lv, H.; Sumliner, J. M.; Zhu, G.; Luo, Z.; Musaev, D. G.; Geletii, Y. V.; Hill, C. L. Differentiating Homogeneous and Heterogeneous Water Oxidation Catalysis: Confirmation that $[Co_4(H_2O)_2(\alpha\text{-}PW_9O_{34})_2]^{10-}$ Is a Molecular Water Oxidation Catalyst. *J. Am. Chem. Soc.* **2013**, *135*, 14110−14118.
(73) Folkman, S. J.; Kirner, J. T.; Finke, R. G. Cobalt Polyoxometalate $Co_4V_2W_{18}O_{68}^{10-}$: A Critical Investigation of Its Synthesis, Purity, and Observed ^{51}V Quadrupolar NMR. *Inorg. Chem.* **2016**, *55*, 5343−5355.
(74) Sullivan, K. P.; Wieliczko, M.; Kim, M.; Yin, Q.; Collins-Wildman, D. L.; Mehta, A. K.; Bacsa, J.; Lu, X.; Geletii, Y. V.; Hill, C. L. Speciation and Dynamics in the $[Co_4V_2W_{18}O_{68}]^{10-}$/ $Co(II)_{aq}$ / CoC_x Catalytic Water Oxidation System. *ACS Catal.* **2018**, *8*, 11952−11959.
(75) *Critical Stability Constants: First Supplement*. Springer US: New York, 1982; Vol. *5*, p 604, Martell, A. E.; Smith, R. M., Eds.
(76) Lv, H.; Song, J.; Geletii, Y. V.; Vickers, J. W.; Sumliner, J. M.; Musaev, D. G.; Kögerler, P.; Zhuk, P. F.; Bacsa, J.; Zhu, G.; Hill, C. L. An Exceptionally Fast Homogeneous Carbon-free Cobalt-based Water Oxidation Catalyst. *J. Am. Chem. Soc.* **2014**, *136*, 9268−9271.
(77) Haschke, S.; Mader, M.; Schlicht, S.; Roberts, A. M.; Angeles-Boza, A. M.; Barth, J. A. C.; Bachmann, J. Direct oxygen isotope effect identifies the rate-determining step of electrocatalytic OER at an oxidic surface. *Nat. Commun.* **2018**, *9*, 1−8.
(78) Dau, H.; Limberg, C.; Reier, T.; Risch, M.; Roggan, S.; Strasser, P. The Mechanism of Water Oxidation: From Electrolysis via Homogeneous to Biological Catalysis. *ChemCatChem* **2010**, *2*, 724−761.
(79) Man, I. C.; Su, H.-Y.; Calle-Vallejo, F.; Hansen, H. A.; Martínez, J. I. M.; Inoglu, N. G.; Kitchin, J.; Jaramillo, T. F.; Nørskov, J. K.; Rossmeisl, J. Universality in Oxygen Evolution Electrocatalysis on Oxide Surfaces. *ChemCatChem* **2011**, *3*, 1159−1165.
(80) Richens, D. T., *The Chemistry of Aqua Ions: Synthesis, Structure, and Reactivity: A Tour through the Periodic Table of the Elements*. John Wiley & Sons: Chichester, 1997; p 592.
(81) Abu-Shandi, K.; Al-Wedian, F. Estimation of composition, coordination model, and stability constant of some metal/phosphate complexes using spectral and potentiometric measurements. *Chem. Papers* **2009**, *63*, 420−425.
(82) Lv, H.; Guo, W.; Wu, K.; Chen, Z.; Bacsa, J.; Musaev, D. G.; Geletii, Y. V.; Lauinger, S. M.; Lian, T.; Hill, C. L. A Noble-Metal-Free, Tetra-nickel Polyoxotungstate Catalyst for Efficient Photocatalytic Hydrogen Evolution. *J. Am. Chem. Soc.* **2014**, *136*, 14015−14018.
(83) Vickers, J. W.; Sumliner, J. M.; Lv, H.; Morris, M.; Geletii, Y. V.; Hill, C. L. Collecting meaningful early-time kinetic data in homogeneous catalytic water oxidation with a sacrificial oxidant. *Phys. Chem. Chem. Phys.* **2014**, *16*, 11942−11949.
(84) Zhao, Y.; Truhlar, D. G. A new local density functional for main-group thermochemistry, transition metal bonding, thermochemical kinetics, and noncovalent interactions. *J. Chem. Phys.* **2006**, *125*, 194101.
(85) Barone, V.; Cossi, M. Quantum Calculation of Molecular Energies and Energy Gradients in Solution by a Conductor Solvent Model. *J. Phys. Chem. A* **1998**, *102*, 1995−2001.
(86) Grimme, S.; Antony, J.; Ehrlich, S.; Krieg, H. A consistent and accurate ab initio parametrization of density functional dispersion correction (DFT-D) for the 94 elements H-Pu. *J. Chem. Phys.* **2010**, *132*, 154104.
(87) Frisch, M. J.; Trucks, G. W.; Schlegel, H. B.; Scuseria, G. E.; Robb, M. A.; Cheeseman, J. R.; Scalmani, G.; Barone, V.; Mennucci, B.; Petersson, G. A.; Nakatsuji, H.; Caricato, M.; Li, X.; Hratchian, H. P.; Izmaylov, A. F.; Bloino, J.; Zheng, G.; Sonnenberg, J. L.; Hada, M.; Ehara, M.; Toyota, K.; Fukuda, R.; Hasegawa, J.; Ishida, M.; Nakajima, T.; Honda, Y.; Kitao, O.; Nakai, H.; Vreven, T.; Montgomery, J. A.; Peralta, J. E.; Ogliaro, F.; Bearpark, M.; Heyd, J. J.; Brothers, E.; Kudin, K. N.; Staroverov, V. N.; Kobayashi, R.; Normand, J.; Raghavachari, K.; Rendell, A.; Burant, J. C.; Iyengar, S. S.; Tomasi, J.; Cossi, M.; Rega, N.; Millam, J. M.; Klene, M.; Knox, J. E.; Cross, J. B.; Bakken, V.; Adamo, C.; Jaramillo, J.; Gomperts, R.; Stratmann, R. E.; Yazyev, O.; Austin, A. J.; Cammi, R.; Pomelli, C.; Ochterski, J. W.; Martin, R. L.; Morokuma, K.; Zakrzewski, V. G.; Voth, G. A.; Salvador, P.; Dannenberg, J. J.; Dapprich, S.; Daniels, A. D.; Farkas, Ö.; Foresman, J. B.; Ortiz, J. V.; Cioslowski, J.; Fox, D. J. *Gaussian 09 Revision E.01*, 2013.

https://doi.org/10.1021/acs.inorgchem.2c00446
Inorg. Chem. 2022, 61, 6252−6262